ACSNANO

www.acsnano.org

ARTICLE

High-Density, Localized Quantum Emitters in Strained 2D Semiconductors

Gwangwoo Kim, Hyong Min Kim, Pawan Kumar, Mahfujur Rahaman, Christopher E. Stevens, Jonghyuk Jeon, Kiyoung Jo, Kwan-Ho Kim, Nicholas Trainor, Haoyue Zhu, Byeong-Hyeok Sohn, Eric A. Stach, Joshua R. Hendrickson, Nicholas R. Glavin, Joonki Suh, Joan M. Redwing, and Deep Jariwala*

Cite This: *ACS Nano* 2022, 16, 9651−9659

Read Online

ACCESS | Metrics & More | Article Recommendations | Supporting Information

ABSTRACT: **Two-dimensional chalcogenide semiconductors have recently emerged as a host material for quantum emitters of single photons. While several reports on defect- and strain-induced single-photon emission from 2D chalcogenides exist, a bottom-up, lithography-free approach to producing a high density of emitters remains elusive. Further, the physical properties of quantum emission in the case of strained 2D semiconductors are far from being understood. Here, we demonstrate a bottom-up, scalable, and lithography-free approach for creating large areas of localized emitters with high density (~150 emitters/um^2) in a WSe_2 monolayer. We induce strain inside the WSe_2 monolayer with high spatial density by conformally placing the WSe_2 monolayer over a uniform array of Pt nanoparticles with a size of 10 nm. Cryogenic, time-resolved, and gate-tunable luminescence measurements combined with near-field luminescence spectroscopy suggest the formation of localized states in strained regions that emit single photons with a high spatial density. Our approach of using a metal nanoparticle array to generate a high density of strained quantum emitters will be applied to scalable, tunable, and versatile quantum light sources.**

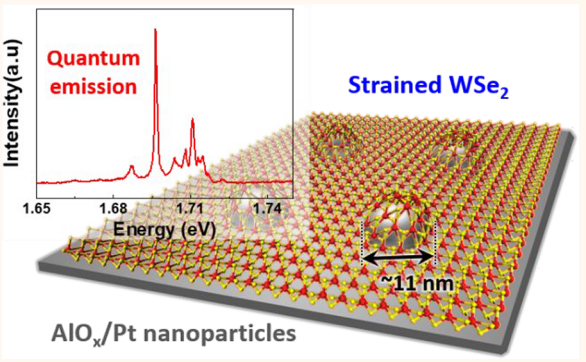

KEYWORDS: *transition metal dichalcogenides, tungsten diselenide, strain engineering, platinum nanoparticles, quantum emitter*

INTRODUCTION

Strain engineering and physical confinement transformation engineering of three-dimensional (3D) semiconductors have been studied either for bandgap engineering or the confinement of discrete quantum states for quantum information processing.[1−3] Importantly, the utilization of local strain for generating quantum confinement has been achieved extensively in III−V semiconducting quantum dots,[4,5] nanowires,[2] and nanotubes.[6] Recently, such studies have been extended to two-dimensional (2D) materials, primarily in insulating hexagonal boron nitride[7−10] and semiconducting transition metal dichalcogenides (TMDCs).[11−14] 2D materials provide a promising platform for strain engineering due to their structural properties. Their strong in-plane bonding makes them amenable to heterointegration with arbitrary substrates that contain other optical/photonic nanostructures. This implies that strain can be readily tuned *via* the substrate topography. To achieve this, Si-based nanopillars[15−18] have been widely used as 3D templates (substrates) to induce such localized strains. Moreover, as these mechanical strains can strongly control band structure, it is possible to use mechanical strain to tune electronic and photonic performance.[19,20] For this reason, the identification of quantum emitters (QEs) in TMDCs has generated considerable excitement in the field of 2D nanophotonics[21−23] and quantum information science and engineering.[24] Despite these intriguing properties, the fundamental origin of quantum emission in TMDCs is not completely clear, and thus far, it is believed that emissions are formed by excitons bound to defects,[12−14] impurities,[11] or 3D transformations (nanostructures, nanoindents) induced by the strain gradients.[15−18,25−28] In addition to this fundamental question, there is a need to create a high spatial and number density of quantum emitters in 2D semiconductors. The high

Received: March 25, 2022
Accepted: May 23, 2022
Published: May 27, 2022

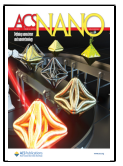

https://doi.org/10.1021/acsnano.2c02974
ACS Nano 2022, 16, 9651−9659

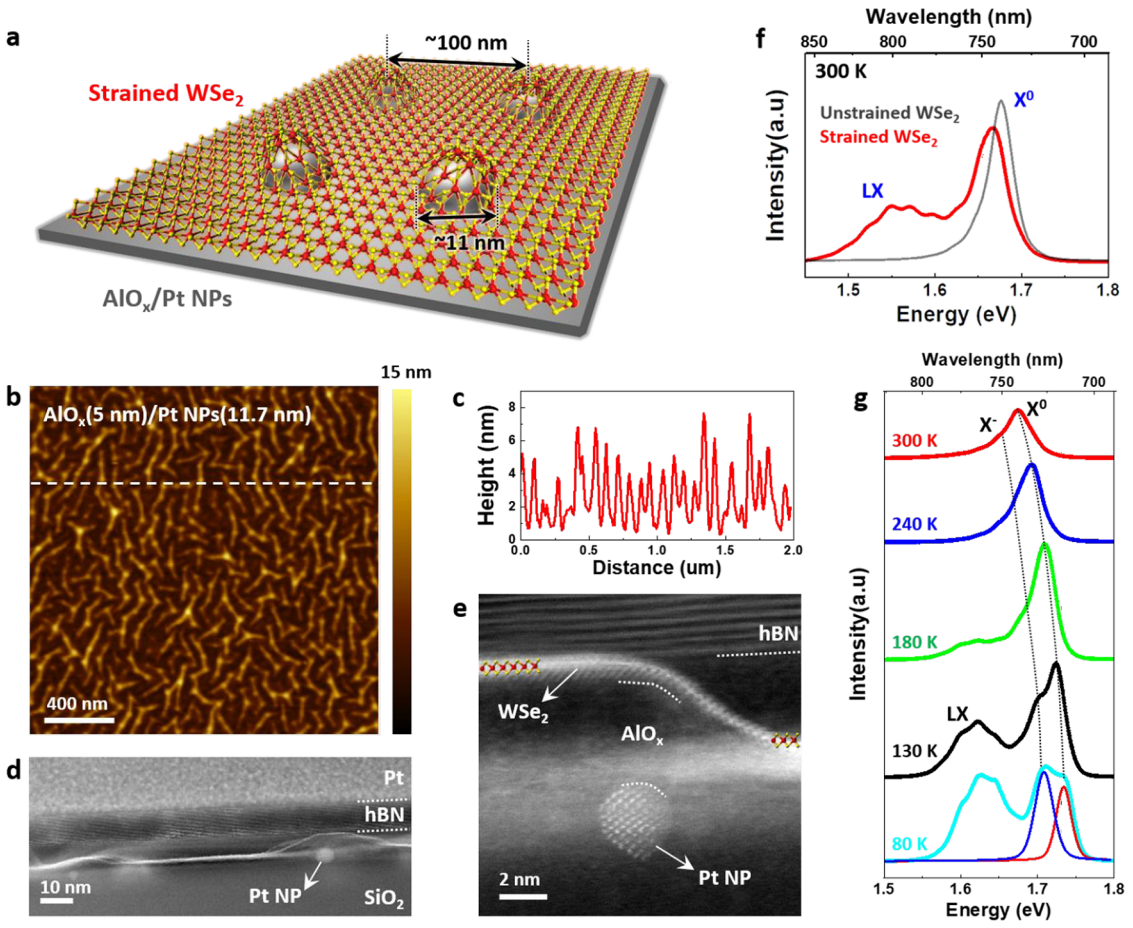

Figure 1. Structural characterization and observation of localized emission in strained ME WSe_2 monolayers. (a) Schematic depiction of a strained WSe_2 monolayer on an AlO_x/Pt NP array with the relevant dimensions labeled. (b) AFM height image of a strained WSe_2 monolayer on AlO_x(5-nm-thick)/Pt NPs(11.6-nm-size). (c) Height profile marked with the white line in (b). (d, e) Representative cross-sectional STEM images of the strained WSe_2 monolayer with h-BN protecting layers clearly showing the curved topography that induces local strain as well as the buried Pt NP with visible atomic columns. (f) Room-temperature PL spectra of strained (red) and unstrained (black) WSe_2, placed on AlO_x(5 nm)/Pt NPs/SiO_2 and a bare SiO_2 substrate, respectively. These spectra were obtained by 405-nm-laser excitation and a 100× lens with 0.9 NA. (g) Temperature-dependent PL spectra of strained WSe_2 on AlO_x(5 nm)/Pt NPs/SiO_2. These spectra were obtained by 405-nm-laser excitation and a 50× lens with 0.35 NA.

number density and high brightness of individual quantum emitters are needed to create dense integration of quantum light sources with other photonic elements in scalable applications.

Here, we demonstrate an approach to forming strain-induced localized quantum emitters with high spatial density (>150/um^2) in a 2D TMDC monolayer that is placed on top of an array of uniform metal nanoparticles (NPs) with AlO_x dielectric layers using a top-down lithography-free approach. We observe localized exciton (LX) emission from the Pt NP-strained WSe_2 structures by using far-field photoluminescence (PL) spectroscopy at room temperature. In addition, we perform a systematic study that combines low-temperature far-field and room-temperature near-field PL spectroscopy to arrive at a mechanistic understanding of the LX emission from strained WSe_2. We conclude that the LX emission originates from the radiative emission control of dark excitons by compressive strain. We also demonstrate an identical LX emission in a large-area WSe_2 monolayer grown by metal organic chemical deposition (MOCVD), which is spatially controllable by using a lithographically patterned array of Pt NPs. Cryogenic and time-resolved PL measurements suggest lifetimes of ~11 ns and with <0.7 nm spectral line widths of emission, which further confirms that our samples have a high density of single-photon emitters formed by a top-down, lithography-free process.

RESULTS AND DISCUSSION

Fabrication of Local-Strained WSe_2 Monolayer and Its Characterization. The WSe_2 monolayers are transferred over a uniform array of Pt NPs deposited with a thin AlO_x spacer. The sample configuration and a schematic of the fabrication process are illustrated in Figure 1a and Figure S1, respectively. The thin AlO_x layer was first deposited on an array of Pt NPs spread over a SiO_2/Si substrate, prepared with the aid of self-patterning diblock copolymer micelles.[29] The Pt NPs were synthesized by spin-coating a single layer of polystyrene-*block*-poly(4-vinylpyridine) (PS-P4VP) micelles with a hexachloroplatinic acid (H_2PtCl_6) precursor for Pt NPs within their cores, followed by annealing at 400 °C. Depending on the molecular weight of the diblock copolymer, the size of the Pt NPs was further controlled to two different sizes with average diameters of 11.7 and 5.9 nm (see Figures S2 and S3a,b for additional characterization). Most of the

https://doi.org/10.1021/acsnano.2c02974
ACS Nano 2022, 16, 9651−9659

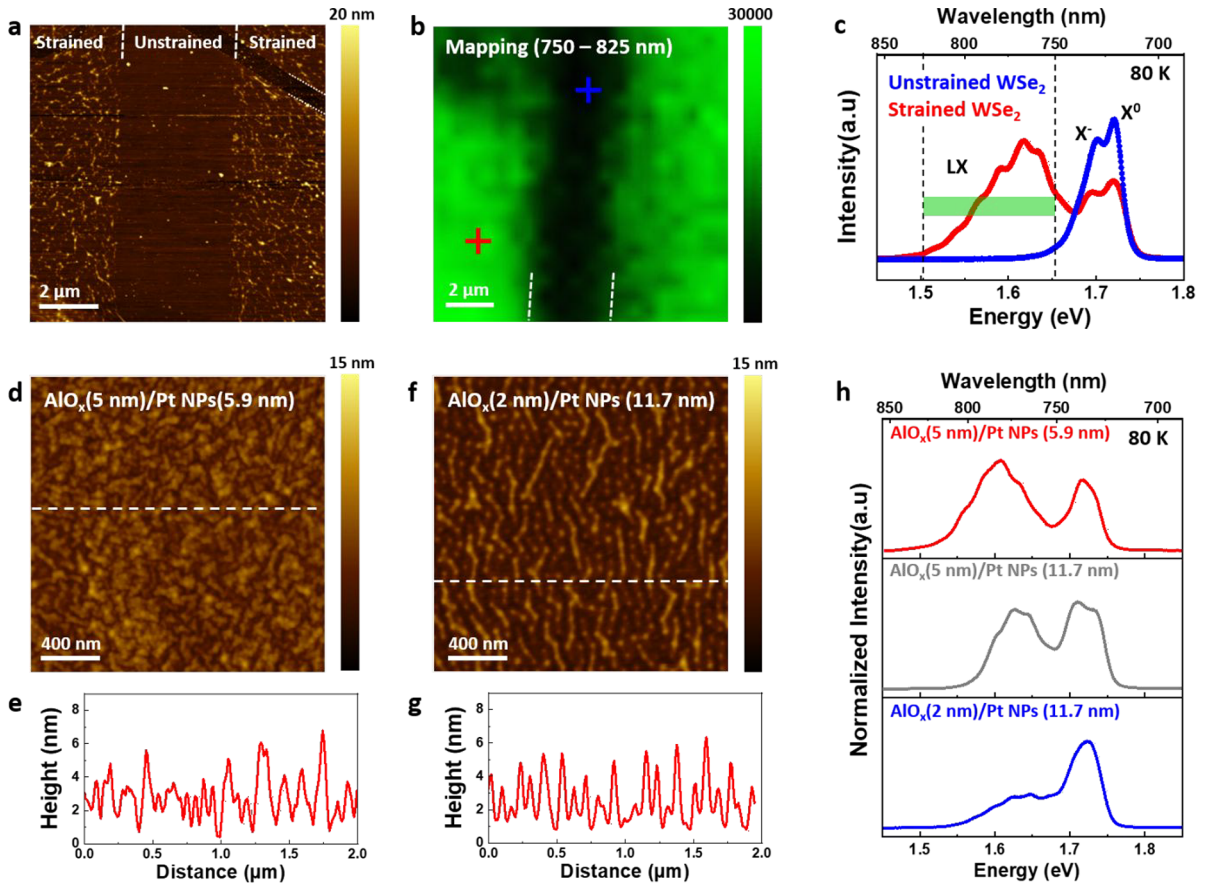

Figure 2. Spatial- and magnitude-controllable localized emission in a strained WSe_2 monolayer by a patterned Pt NP array. (a) AFM height image of an MOCVD-grown WSe_2 monolayer placed on the stripe-patterned Pt NP array with 5-nm-thick AlO_x. (b) Far-field PL mapping of localized emission energy (integrated intensity of 750−825 nm) at 80 K. (c) PL spectra from the corresponding points marked with blue (unstrained WSe_2) and red (strained WSe_2) crosses in (b). (d, f) AFM height images of strained ME WSe_2 monolayers on (d) AlO_x(5 nm)/small Pt NPs(5.9 nm)/SiO_2 and (f) AlO_x(2 nm)/large Pt NPs(11.7 nm)/SiO_2. (e, g) Height profiles marked with the white line in the (d) and (f). (h) Low-temperature PL spectra of strained ME WSe_2 monolayers on each substrate.

results discussed below were obtained on an 11.7-nm-sized Pt NP array with an average interparticle distance of 103 nm. Upon synthesis of the array of Pt NPs, we deposited a thin layer of AlO_x (2, 5 nm thickness, Figure S3c−f) for use as a spacer *via* atomic layer deposition (ALD). This spacer layer is necessary to prevent the quenching of excitons in 2D TMDCs *via* direct contact with metallic Pt NPs. It is worth noting that thicker AlO_x depositions result in larger height differences between the top of Pt NPs and the substrate, suggesting preferential ALD growth of AlO_x on the Pt NPs. Following ALD AlO_x deposition, either mechanically exfoliated (ME) or MOCVD-grown WSe_2 monolayers were transferred onto the AlO_x-deposited Pt NP arrays by either a pick-up (for exfoliated crystals) or a wet-transfer (for MOCVD-grown films) method. Finally, the as-prepared samples were annealed at 300 °C with Ar flow (50 sccm) in a vacuum tube furnace to make better conformal contact by removing trapped solvent or gas molecules at the interface between the WSe_2 and AlO_x/Pt NPs substrate. Structural characterization of locally strained WSe_2 on AlO_x/Pt NP arrays after annealing was performed by atomic force microscopy (AFM) (Figure 1b,c) and scanning transmission electron microscopy (STEM) (Figure 1d,e and Figures S4, S5), respectively. As shown in Figure 1b, we clearly observe visible wrinkles between NPs, indicating deformation and strain in the WSe_2 monolayers. Atomically resolved STEM images (Figure 1e) and energy dispersive X-ray spectroscopic (EDS) elemental mapping (Figure S5) show that the WSe_2 monolayer is conformal to the AlO_x-covered Pt NP array, which is direct evidence that a locally strained structure has been created.

The effect of local strain on the prepared ME WSe_2 monolayer is examined by micro-PL spectroscopy with a 405 nm excitation laser. Figure 1f compares the representative PL spectra of the locally strained WSe_2 (red) and unstrained WSe_2 (black) layers, measured with a 100× lens (0.9 numerical aperture, NA) at room temperature. As reported in literature precedents,[17,30,31] the strained WSe_2 exhibits a clear redshift (~30 meV) of the neutral exciton (X^0) peak (1.66 eV), considering that this shifting is due to the exciton funneling effect caused by strain, which entails a reduction in the average bandgap as obtained *via* a far-field optical measurement. We note, however, that the strain is spatially nonuniform in our system, which therefore makes it difficult to assign a bandgap to the sample unless a spatial scale is specified since the bandgap is spatially varying on the scale of tens of nanometers due to inhomogeneous strain. From the magnitude of the redshift (X^0) and the theoretical calculation,[32] we estimate our strained WSe_2 samples are subjected to approximately 0.38 ± 0.021% biaxial tensile strain. The presence of strain in the WSe_2 was confirmed by micro-Raman spectroscopy (Figure S6). The strained WSe_2 sample (Figure S6a) shows a significant redshift of 0.65 cm^{-1} for the E_{2g}/A_{1g} Raman peak,

https://doi.org/10.1021/acsnano.2c02974
ACS Nano 2022, 16, 9651−9659

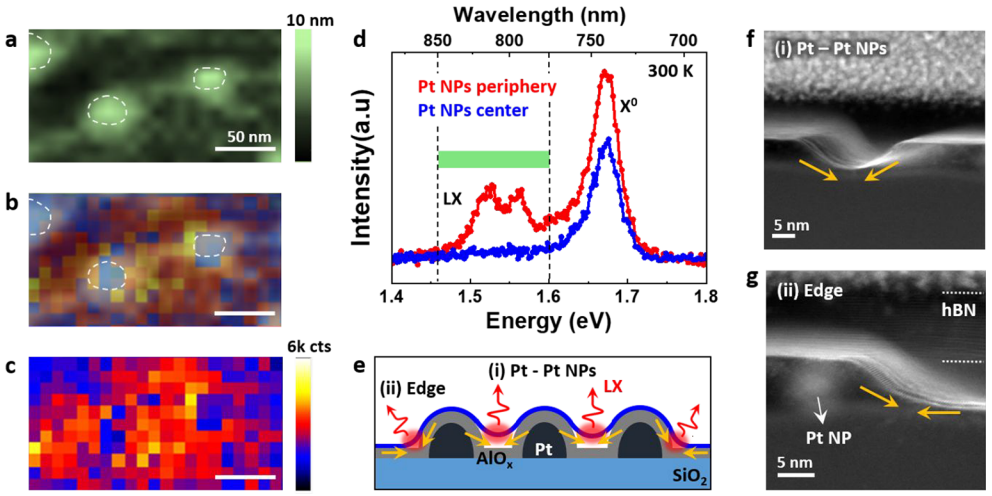

Figure 3. Nanoscale optical and structural imaging of localized emission on strained WSe_2. (a–c) AFM height image (a) and corresponding TEPL spatial map (c) of strained WSe_2 monolayer on AlO_x(2 nm)/Pt NPs/SiO_2. The TEPL image was created within the spectral range of 770–850 nm with a step size of 10 nm. The excitation energy was 1.96 eV (633 nm). (b) Overlaid image of (a) and (c). (d) TEPL spectra of a WSe_2 monolayer on Pt NPs' center (blue) and periphery (red) as highlighted in the TEPL map. The clear differences in emission spectra at the LX peaks (1.45–1.6 eV energy range) is evident. (e) Schematic diagram of the sample cross-section showing the position of localized emissions. (f, g) Cross-sectional STEM images of strained WSe_2 showing the two cases of the curved WSe_2 monolayers under compressive strain: (i, f) between the top of Pt NPs or (ii, g) in contact with the flat substrate.

again indicating ~0.35 ± 0.034% biaxial tensile strain,[17] in good agreement with the strain values derived from PL peak shifts above. We further confirmed the strain effect *via* Raman spectroscopy in another TMDC: WS_2 (Figure S6b). In that case, the in-plane E_{2g} mode also shows a similar strain-dependent redshift, whereas the out-of-plane A_{1g} mode showed negligible shift under applied strain. Note that these tensile strains are concentrated on top of Pt NPs and compressive strain may be formed between the NPs. This will be discussed in more detail below. Interestingly, we observe an LX emission in our strained samples, in addition to the X^0 emission (Figure 1f, red curve). The energies of the observed LX emission (1.4–1.55 eV) are lower than that of X^0 (1.63 eV), similar to the recently reported results for WSe_2 nanobubbles.[33] Figure 1g presents the temperature-dependent PL spectra of the strained WSe_2 monolayer on the AlO_x(5 nm)/Pt NP array. Note that the LX peak, as seen in Figure 1f, red curve, at room temperature, was not visible in the room-temperature spectrum (red) in Figure 1g because of the instrumental configuration, which utilized a long-distance 50× lens (0.35 NA) for variable-temperature measurements in a vacuum and at cryogenic stage. However, we still clearly observed the LX peaks in the 1.6–1.65 eV range at low temperature (80 K), while no LX emission was observed in the unstrained WSe_2 on a bare SiO_2/Si substrate (Figure S7) across the entire temperature range. Similarly, the LX emission was also confirmed in an MOCVD-grown WSe_2 monolayer formed over the entire area, shown in Figure S8. This demonstrates the potential of large-area scalability by also utilizing CVD-grown TMD monolayers with continuous single-crystallinity and uniformity.[34]

Spatial- and Magnitude-Controllable Localized Emission in a Strained WSe_2 Monolayer. The above observations, particularly in MOCVD-grown WSe_2, suggest that it is possible to pattern regions showing LX emissions over a large area. Since the strain and the resulting LX emission from the TMDC are highly dependent on the substrate topography, it can be spatially controlled by patterning the Pt NP array on the substrate. To demonstrate this, we prepared stripe-patterned arrays of Pt NPs on a substrate using photolithography to mask and selectively etch Pt NPs with an *aqua regia* solution (Figure S9) in the exposed regions. Then, after depositing the AlO_x thin layer by ALD, an MOCVD-grown WSe_2 monolayer was transferred to the patterned substrate and annealed in the same conditions as discussed above. Figure 2a shows AFM height images of the alternating strained/unstrained MOCVD-WSe_2 films. As shown in the magnified image (Figure 2b), the presence and absence of a Pt NP array is clearly identified. To verify the origin of the LX emission, we performed a far-field PL analysis at an 80 K temperature. Notably, the PL mapping image (Figure 2c) in the range of 750–825 nm clearly confirms that the LX emission is only detected in the strained WSe_2 area. The red and blue lines in Figure 2d show the corresponding PL spectra of the strained and unstrained regions, respectively. These results provide clear evidence that the origin of the LX peak in emission is related to the strain effect on the WSe_2 monolayer.

To understand the strain effect and its relation to the LX emission, we performed low-temperature PL measurements on several control samples. First, we note that although there is a distinct possibility that defects or inducing impurities are formed in the WSe_2 during the annealing treatment, no LX emission was observed in the unstrained WSe_2 sample on a flat SiO_2/Si substrate (Figure S7), which was annealed and went through the same treatments as the strained samples. Second, it is also plausible that the origin of the LX peak might be due to either charge-trapped sites in the AlO_x dielectric layer or hybridization of localized surface plasmons in the Pt NPs with excitons in WSe_2. To verify that these effects were not contributing to this system, we prepared two kinds of control WSe_2 samples: on (i) an AlO_x-deposited SiO_2 substrate without Pt NPs (Figure S10) and (ii) a pristine Pt NP array/SiO_2 substrate (Figure S11). The LX emission was not observed in either sample. Sample (i) at low temperatures showed no visible LX emission, while in sample (ii), the PL emission completely disappeared due to direct contact

https://doi.org/10.1021/acsnano.2c02974
ACS Nano 2022, 16, 9651–9659

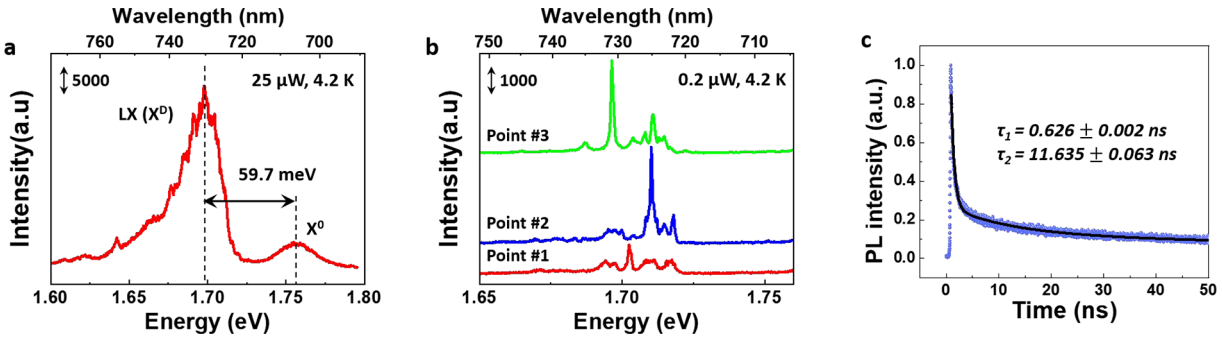

Figure 4. Cryogenic PL and time-resolved PL (TRPL) measurement. (a, b) PL spectra of a strained WSe_2 monolayer with a pulse laser excitation (637 nm, 1 MHz) with an excitation power of (a) 25 and (b) 0.2 μW at 4.2 K. (c) TRPL spectra of the localized emission. The time-resolved PL data (red dotted lines) are convoluted (black solid lines) with the instrument response function, using a biexponential function $I = A_1 \exp(-t_1/\tau_1) + A_2 \exp(-t_2/\tau_2)$.

between WSe_2 and metallic Pt after annealing, which resulted in quenching of the emission. In addition to Pt NPs, we prepared the strained WSe_2 monolayer on top of a 3D template based on the Au NP array with similar size and spacing and observed identical LX emission to that on Pt NPs. (See Figure S12 and Figure S13 in the Supporting Information for additional details.) These control experiments further confirm that the LX emission is likely due to the local strain effect in the WSe_2 monolayers.

Given that our strain-inducing agent is an array of Pt NPs, this results in the ability to control these local strains by varying the size and spacing of Pt NPs and the deposition thickness of the AlO_x layer. Inducing these changes in the substrate topography allows altering the intensity change of LX emission. Figure 2d shows the strained WSe_2 monolayer on AlO_x (5-nm-thick)/Pt NPs with a smaller size (5.9 nm) and spacing (51 nm) (Figure 2b). As shown in the AFM height images, we observed that the surface was relatively nonuniform and congested compared to the previous AlO_x(5 nm)/Pt NPs (11.7 nm) sample (Figure 1b). Smaller and denser Pt NP arrays created stronger and denser strain, leading to an enhanced LX emission (Figure 2h). Next, as mentioned previously (Figure S3), the height of the Pt NPs could be changed by controlling the AlO_x thickness during the deposition process, which is expected to affect the strain in the WSe_2 monolayer placed on top. Figure 2f shows an AFM image of a strained WSe_2 monolayer on AlO_x (2 nm)/Pt NPs (11.7 nm). This sample had a relatively smooth surface, and, as a result, LX emission with a smaller intensity was observed at 80 K. Also, the LX peaks tended to shift to slightly lower energy with increasing strain. This will be discussed in more detail later.

Nano-optical Imaging and Spectroscopic Analysis of Localized Emissions in Strained WSe_2. The far-field PL spectroscopic results between room temperature and 80 K described above show that the observed LX emission is due to strain in the WSe_2 monolayer induced by the Pt NP array substrate. To verify the spatial position of LX emission and mechanistically understand the origin of the LX emission,[33,35] we performed tip-enhanced PL spectroscopy (TEPL) on our samples with a 633-nm-excitation laser and a spatial resolution of ~10 nm. Figure 3 displays TEPL results on the strained WSe_2 monolayer on an AlO_x(2 nm)/Pt NPs/SiO_2 substrate. Note that TEPL measurement was carried out at room temperature and a relatively thin AlO_x layer (2 nm) was deposited to allow strong confinement of the gap-plasmon mode between the tip and the underlying Pt NPs such that the PL signal from the WSe_2 monolayer sandwiched between the Au tip and Pt NPs is enhanced by virtue of the gap plasmonic cavity. As shown in the AFM height image (Figure 3a), WSe_2 flexure is distributed with a size of <25 nm on the surface. Figure 3d contrasts the TEPL spectra collected from the region of the WSe_2 monolayer center above a Pt NP (blue) from the periphery (red) (more spectra on several positions are provided in Figure S14). The blue spectrum of the Pt NPs' center is composed of the typical PL emission of a WSe_2 monolayer with a neutral exciton (X^0) peak. The red spectrum measured around the Pt NPs is noticeably different, exhibiting the LX emission, similar to the previously shown far-field PL spectrum (red, Figure 1f). Interestingly, the corresponding TEPL map (Figure 3c) in the range of 775−850 nm shows that the LX emission is localized to a concentric ring around the Pt NPs rather than on top of the NP, where the tensile strain is largest. This implies that compressive strains (yellow arrows) formed on the curved WSe_2 monolayer (i) between the top of Pt NPs or (ii) in contact with the flat substrate may be the likely cause of the LX emission (Figure 3e). These compressive strain regions are also visible in the cross-sectional TEM images (Figure 3f,g), and each image clearly shows the two cases (i: Figure 3f, ii: Figure 3g) mentioned above. Furthermore, the strain can be confirmed by comparing the aforementioned AFM height profiles of AlO_x-deposited Pt NPs (Figure S3f) and WSe_2 transferred on the top (Figure 1c). The difference between the highest and lowest heights decreased from 11.19 ± 1.57 nm to 6.07 ± 1.02 nm after transferring WSe_2. This indicates that the WSe_2 monolayer is freestanding and in a bent state between the Pt NPs under compressive strain.

To get a deeper insight into the origin of the features, we have also compared the presence or absence of the LX emission in other TMDCs and only observed the LX emissions in W-based TMDCs and not in Mo-based TMDCs (see Figure S15 for additional details). From these results, we could speculate that the origin of the LX emission might be associated with the dark exciton in TMDCs. It is well known that in Mo- and W-based TMDC layers, the strong spin−orbit coupling can induce the band splitting of both the conduction and valence bands into two sub-bands with opposite spins, thereby producing dark exciton states.[36−38] In the case of W-based TMDCs, these dark excitons can be easily detected in optical measurements since the dark exciton state is located energetically below the bright exciton state and is, therefore,

https://doi.org/10.1021/acsnano.2c02974
ACS Nano 2022, 16, 9651−9659

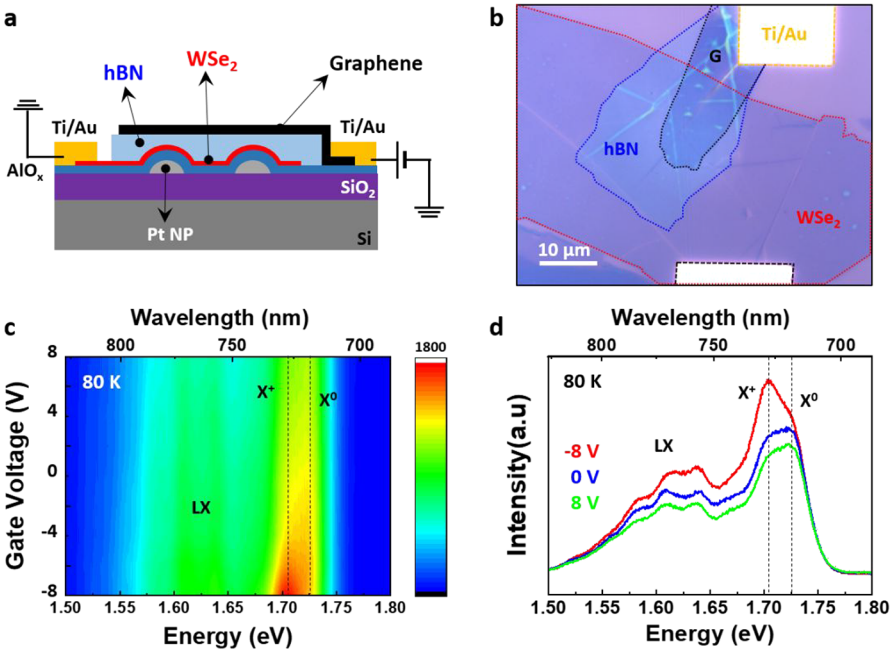

Figure 5. Gate-dependent PL spectroscopy of the strained WSe_2 device. (a, b) Schematic (a) and optical microscopic image (b) of the strained WSe_2 device with hBN dielectric layers and graphene top gate electrode. (c) PL spectra of WSe_2 at 80 K as a function of the top gate voltage. The color represents the PL intensity. (d) PL spectra at the top gate voltage of +8, −8, and 0 V.

the ground state of the exciton. In contrast, in Mo-based TMDCs, the bright exciton forms the ground state. Further, the bands in W-based TMDCs have a relatively large band splitting (40−50 meV), in comparison with Mo-based TMDCs (∼10 meV).[39−41] It is noteworthy that the dark−bright band splitting in our strained W-based TMDCs has a relatively large value of ∼80 meV. According to a recent theoretical paper,[42] the aforementioned compressive strain in TMDC monolayers enables not only to increase the dark−bright state separation value but also to enhance the intensity of the dark exciton. This trend is clearly visible in the magnitude-controlled LX results introduced earlier (Figure 2h). When Pt NPs with a smaller size and narrower spacing were used, or when the ALD deposited AlO_x layer was thicker , a larger compressive strain could be induced in the WSe_2 monolayer, making the LX peak stronger and shifting it to lower energies. In addition, we also perform excitation power-dependent PL measurements to determine that the cause of the LX emission is dark excitons (see Figure S16 for additional details). Since the intensity of the dark excitons should obey a linear dependence as a function of incident power, the power dependence is an excellent indicator for dark excitons.[41,43]

In addition to near-field PL, we also performed far-field cryogenic PL (down to 4.2 K) and time-resolved PL (TRPL) measurements to directly probe the LX emission dynamics. Figure 4a,b shows the PL spectra on the strained WSe_2 monolayer, which was obtained with a pulsed excitation laser (637 nm, 1 MHz) with 25 and 0.2 μW power at 4.2 K. As seen in the PL spectrum acquired under a high-power laser (Figure 4a), both X^0 (bright excitons) and LX emissions (dark excitons) are now clearly visible. The energy difference between X^0 and LX is measured to be 59.7 meV, which is higher than the previously reported values.[39−41,44] As mentioned above, relatively large splitting originates from the radiative emission control of the dark excitons by compressive strain.[42] Although at high excitation power the single phone peaks are hidden by the high background signal, we could observe the sharp LX emission with narrow line widths (524 ± 102 μeV) at low power (Figure 4b), and they originate from the dark excitons trapped in the strain-induced potential as discussed above. These sharp emission lines resemble single-photon emitters from dark exciton and defect states in TMDCs, as reported in several prior studies. While the 4.2 K PL spectra reveal sharp emission peaks indicating possible single-photon emitters, to obtain another confirmation, we performed TRPL analysis (Figure 4c) by selecting a wavelength range in the PL signal (dashed lines marked in Figure S17) using band-pass filters. A biexponential fit to the decay data trace shows two decay components, fast (τ_1) and slow (τ_2). The slow component (τ_2) exhibits 2 orders of magnitude longer lifetime than the fast component (τ_1). Given the low pumping (excitation) power employed in this measurement, the LX-state lifetime close to 11 ns corresponds to the range of previously reported lifetime values (8−12 ns)[16] of single-photon emission in WSe_2. To further confirm single-photon emission, we attempted to perform a second-order photon-correlation measurement ($g^{(2)}$) on several points on the sample. However, the large spatial density of emitters (∼150/um^2) within the excitation spot size prevents the isolation of a single emitter from providing a reliable $g^{(2)}$ measurement. Nevertheless, on the basis of the lifetimes and the multiple narrow line width emission lines emanating from the broader inhomogeneous line width PL spectra at low temperatures, we can indeed point to a structure with a high spatial density of single-photon emitters. Similar narrow line width emission signals were observed in the strained WS_2 monolayer fabricated with the same structure (Figure S18), indicating that the current system can be universally applied to other 2D semiconductors with a dark ground state exciton.

Finally, if the strain-induced localization of exciton states is indeed true, these states should also be amenable to the electrostatic gate-induced tuning of the emission. To verify

https://doi.org/10.1021/acsnano.2c02974
ACS Nano 2022, 16, 9651−9659

this, we fabricated a strained WSe_2 device encapsulated with hexagonal boron nitride (hBN) flakes through a pickup method as described previously and shown schematically in Figure 5a. The WSe_2 monolayer is gated through few-layer graphene as the top-gate electrode, with the top BN flake working as the gate dielectric (Figure 5b). Figure 5c,d shows the gate-dependent PL spectra of the strained WSe_2 monolayer measured at 80 K. The PL spectra at specific gate voltages of +8, −8, and 0 V are shown in Figure 5d, and the PL intensities for X^0, X^+, and LX are sensitive to the gate voltage. At the gate voltage of −8 V (red line in Figure 5d), the WSe_2 is strongly p-doped. All the intensities of X^0, the positive trion X^+, and the LX emission increase gradually, while the X^+ peak shows relatively stronger intensity-tunability. At the top gate voltage of +8 V (green line in Figure 5d), the WSe_2 is n-doped and all three peaks (X^0, X^+, LX) are quenched. Especially with the increase of the hole concentration (increasing negative bias), the intensities of X^+ and LX increase more significantly than the neutral excitonic features (X^0), confirming that the LX emission could be attributed to the positively charged dark trion. The above results show that increasing the hole doping level with the top gate voltage is important to enhance the LX emission further. From Figure 5c,d, it is obvious that the spectrum weight of all the resolved excitonic complexes depends sensitively on the top gate voltage, which effectively controls the density and type of charge carriers in the strained WSe_2 monolayer.

CONCLUSIONS

In conclusion, we have demonstrated an approach to fabricating strain-induced localized quantum emitters with high spatial density in a WSe_2 monolayer on a uniform Pt NP array. This strained WSe_2 structure shows LX at room temperature that is significantly red-shifted from both neutral excitons and trions. The sample topography and Pt NP density create compressive strain in spaces between the Pt NPs where the LX emission originates *via* the tuning of dark excitons by compressive strain. Our approach is free of top-down lithography and is highly scalable to large-area TMDCs, as well as demonstrated to be applicable for other 2D semiconductors. Finally, our structure allows observation of quantum emission at low temperature, which is further tunable passively *via* Pt NP size and density as well as actively *via* a gate voltage. Our results, therefore, advance the state of the art in producing a high density of strain-induced, localized quantum emitters in TMDC monolayers in a scalable, controllable, and lithography-free approach, which is critical for future progress in the science and technology of quantum light sources.

METHODS

Sample Preparation. To make a uniform array of Pt (or Au) NPs on a SiO_2 substrate, a single layer of PS-P4VP micelles with hexachloroplatinic acid (H_2PtCl_6) (or tetrachloroauric acid, $HAuCl_4$, for Au NPs) in their cores, a precursor for Pt NPs, was spin-coated on the SiO_2 substrate.[29] The micellar film on the SiO_2 was annealed at 400 °C for 30 min in air. Next, the AlO_x thin layer was deposited on the Pt NP array/SiO_2 substrate by ALD-Cambridge Nanotech (USA), where a metal organic precursor of trimethylaluminum was used with water vapor in each cycle. Then, either an ME or an MOCVD-grown WSe_2 monolayer was transferred onto the AlO_x-deposited Pt NP arrays by a pick-up or a wet-transfer method. ME-WSe_2 monolayers were exfoliated from bulk crystal (HQ-graphene) using Scotch tape, and MOCVD-grown WSe_2 monolayers were grown in a cold wall vertical reactor with tungsten hexacarbonyl ($W(CO)_6$, Sigma-Aldrich, 99.99% purity) and hydrogen selenide (H_2Se, Matheson, 99.998% purity).[45] Finally, the as-prepared samples were annealed at 300 °C with Ar flow (50 sccm) in a vacuum tube furnace.

Device Fabrication. To make a top gate device, mechanically exfoliated hBN and graphene flakes were sequentially transferred on top of the WSe_2 samples prepared by the above method. Next, the fabrication of Ti (10 nm)/Au (100 nm) electrode contacts was achieved by using electron beam lithography (Elionix ELS-7500EX) and an e-beam evaporator (Kurt J. Lesker PVD-75). Finally, the samples were cleaned in acetone for the lift-off process.

Optical and Structural Characterization. Far-field Raman and PL spectroscopy were performed in a Horiba LabRam HR Evolution confocal microscope with 405 and 633 nm excitation lasers. The signals were collected through the 100× microscope objective (Olympus SLMPLN, NA = 0.90) for room-temperature measurements and a 50× microscope objective (Olympus SLMPLN, NA = 0.35) for low-temperature measurements (up to 80 K). Also, for the low-temperature analysis, samples were placed in a Linkam stage with a liquid nitrogen supply while cooling and heating and pumped to 5×10^{-3} Torr during the measurement. Additionally, for electrostatic gating, the electrical bias was applied using a Keithley 2450 sourcemeter. An OmegaScope Smart SPM (AIST-NT) setup was used for topography scans. For near-field PL measurements, Au-coated OMNI-TERS probes (APP Nano) were used in the identical AFM setup coupled to a far-field Horiba confocal microscope with a 633 nm excitation laser. Time-resolved photoluminescence was measured by using PicoQuant's LDH-I series picosecond laser diodes (IB-470-B, IB-640-B), at a repetition rate according to the lifetime of the system. The PL was spectrally filtered using a pair of Semrock long- and short-pass tunable optical filters and guided into a single-photon avalanche diode (Micro Photon Devices, PDM series). The event timing was recorded using a PicoQuant HydraHarp 400 event timer. The decay of the resulting timing data was then fit with an exponential (mono-, bi-, or triexponential, depending on which gave the best fit) using Origin's fitting software for extracting the PL lifetime. Aberration-corrected high angle annular dark field (HAADF)-STEM and EDS measurements were performed at 200 keV using a JEOL NEOARM microscope. HAADF STEM images were acquired using a 1 Å probe size and a camera length of 4 cm. Images were captured by a Gatan annular detector using Gatan's GMS Software. EDS scanning was performed utilizing a large-area dual detector system. The cross-sectional sample was prepared with a Xe^+ plasma based focused-ion-beam (FIB) system (TESCAN S8000X FIB/SEM). Before cross-sectional sample preparation, the mechanically exfoliated h-BN layer was dry-transferred over the sample area to soft protect the monolayer WSe_2, while an e-beam and ion-beam deposited Pt layer was used further for hard protection to avoid any damage from the FIB processing.

ASSOCIATED CONTENT

Supporting Information

The Supporting Information is available free of charge at https://pubs.acs.org/doi/10.1021/acsnano.2c02974.

Sample fabrication process; SEM and AFM images of a metal NP array; STEM and EDS mapping images; Raman comparison; AFM images and low-temperature PL spectra of control samples (unstrained WSe_2, CVD-grown WSe_2, $WSe_2/AlO_x/SiO_2$, WSe_2/Pt NPs/SiO_2, and WSe_2/AlO_x/Au NPs/SiO_2); additional near-field PL spectra; low-temperature PL spectra of other TMDCs; laser-power-dependent PL spectra; cryogenic PL spectra of strained WSe_2 and WS_2 (PDF)

AUTHOR INFORMATION

Corresponding Author

Deep Jariwala − *Department of Electrical and Systems Engineering, University of Pennsylvania, Philadelphia,*

https://doi.org/10.1021/acsnano.2c02974
ACS Nano 2022, 16, 9651−9659

Pennsylvania 19104, United States; orcid.org/0000-0002-3570-8768; Email: dmj@seas.upenn.edu

Authors

Gwangwoo Kim − *Department of Electrical and Systems Engineering, University of Pennsylvania, Philadelphia, Pennsylvania 19104, United States;* orcid.org/0000-0001-8519-4411

Hyong Min Kim − *Department of Electrical and Systems Engineering, University of Pennsylvania, Philadelphia, Pennsylvania 19104, United States;* orcid.org/0000-0002-0094-4189

Pawan Kumar − *Department of Electrical and Systems Engineering, University of Pennsylvania, Philadelphia, Pennsylvania 19104, United States; Department of Materials Science and Engineering, University of Pennsylvania, Philadelphia, Pennsylvania 19104, United States;* orcid.org/0000-0002-5764-2915

Mahfujur Rahaman − *Department of Electrical and Systems Engineering, University of Pennsylvania, Philadelphia, Pennsylvania 19104, United States*

Christopher E. Stevens − *Air Force Research Laboratory, Sensors Directorate, Wright-Patterson Air Force Base, Ohio 45433, United States; KBR Inc., Beavercreek, Ohio 45431, United States*

Jonghyuk Jeon − *Department of Chemistry, Seoul National University, Seoul 08826, Republic of Korea*

Kiyoung Jo − *Department of Electrical and Systems Engineering, University of Pennsylvania, Philadelphia, Pennsylvania 19104, United States;* orcid.org/0000-0003-4587-234X

Kwan-Ho Kim − *Department of Electrical and Systems Engineering, University of Pennsylvania, Philadelphia, Pennsylvania 19104, United States*

Nicholas Trainor − *2D Crystal Consortium-Materials Innovation Platform, Materials Research Institute, The Pennsylvania State University, University Park, Pennsylvania 16802, United States*

Haoyue Zhu − *2D Crystal Consortium-Materials Innovation Platform, Materials Research Institute, The Pennsylvania State University, University Park, Pennsylvania 16802, United States*

Byeong-Hyeok Sohn − *Department of Chemistry, Seoul National University, Seoul 08826, Republic of Korea*

Eric A. Stach − *Department of Materials Science and Engineering, University of Pennsylvania, Philadelphia, Pennsylvania 19104, United States;* orcid.org/0000-0002-3366-2153

Joshua R. Hendrickson − *Air Force Research Laboratory, Sensors Directorate, Wright-Patterson Air Force Base, Ohio 45433, United States;* orcid.org/0000-0002-5342-0346

Nicholas R. Glavin − *Air Force Research Laboratory, Materials and Manufacturing Directorate, Wright-Patterson Air Force Base, Ohio 45433, United States;* orcid.org/0000-0002-9447-7509

Joonki Suh − *Department of Materials Science and Engineering, Ulsan National Institute of Science and Technology, Ulsan 44919, Republic of Korea;* orcid.org/0000-0002-0221-8447

Joan M. Redwing − *2D Crystal Consortium-Materials Innovation Platform, Materials Research Institute, The Pennsylvania State University, University Park, Pennsylvania 16802, United States;* orcid.org/0000-0002-7906-452X

Complete contact information is available at: https://pubs.acs.org/10.1021/acsnano.2c02974

Author Contributions

G.K. and D.J. conceived the idea/concept. G.K. implemented the project and performed sample preparation with the help of H.M.K, far-field optical (temperature dependence and gate-tunable PL up to 80 K) characterizations with the help of H.M.K and K.H.K, atomic force microscopy, and data analysis. M.R. and K.J. performed near-field PL analysis. P.K. performed cross-sectional sample preparation and STEM characterization under the supervision of E.A.S. and D.J. Cryogenic PL and time-resolved PL measurements at 4.2 K were recorded by C.E.S. under the supervision of J.R.H. J.J. and B.H.S. provided the Pt nanoparticle array on SiO_2 substrates. N.T. and H.Z. prepared and characterized MOCVD-grown WSe_2 samples under the supervision of J.M.R. G.K. and D.J. wrote the manuscript with inputs from all coauthors.

Notes

The authors declare no competing financial interest.

ACKNOWLEDGMENTS

D.J. and G.K. acknowledge primary support for this work by the Air Force Office of Scientific Research (AFOSR) FA2386-20-1-4074 and partial support from FA2386-21-1-4063. D.J., E.A.S., and P.K. acknowledge partial support from National Science Foundation (DMR-1905853) and support from University of Pennsylvania Materials Research Science and Engineering Center (MRSEC) (DMR-1720530) in addition to usage of MRSEC-supported facilities. The sample fabrication, assembly, and characterization were carried out at the Singh Center for Nanotechnology at the University of Pennsylvania, which is supported by the National Science Foundation (NSF) National Nanotechnology Coordinated Infrastructure Program grant NNCI-1542153. K.J. was supported by a Vagelos Institute of Energy Science and Technology graduate fellowship. The large area-MOCVD-WSe_2 monolayer samples were provided by the 2D Crystal Consortium−Materials Innovation Platform (2DCC-MIP) facility at The Pennsylvania State University, which is funded by NSF under cooperative agreement DMR-1539916. J.R.H. acknowledges support from the Air Force Office of Scientific Research (Program Manager Dr. Gernot Pomrenke) under award number FA9550-20RYCOR059. M.R. acknowledges support from Deutsche Forschungsgemeinschaft (DFG, German Research Foundation) for a Walter Benjamin Fellowship (award no. RA 3646/1-1). J.S. acknowledges support by the National Research Foundation of Korea (MSIT) (grant nos. NRF-2020R1C1C1011219 and NRF-2020M3H3A1100938). D.J. and H.-M.K. acknowledge partial support from the Center of Undergraduate Research Fellowships and Class of 1971 Robert J. Holtz Fund Research Grant. N.R.G. acknowledges the support from the Air Force Office of Scientific Research grant FA9550-19RYCOR050.

REFERENCES

(1) Kash, K.; et al. Strain-induced confinement of carriers to quantum wires and dots within an InGaAs-InP quantum well. *Appl. Phys. Lett.* **1989**, *55* (7), 681−683.

(2) Gershoni, D.; et al. Optical transitions in quantum wires with strain-induced lateral confinement. *Phys. Rev. Lett.* **1990**, *65* (13), 1631−1634.

(3) Schülein, F. J. R.; et al. Cascaded exciton emission of an individual strain-induced quantum dot. *Appl. Phys. Lett.* **2009**, *95* (8), 083122.
(4) Buckley, S.; Rivoire, K.; Vučković, J. Engineered quantum dot single-photon sources. *Rep. Prog. Phys.* **2012**, *75* (12), 126503.
(5) Sebald, K.; et al. Single-photon emission of CdSe quantum dots at temperatures up to 200 K. *Appl. Phys. Lett.* **2002**, *81* (16), 2920–2922.
(6) He, X.; et al. Tunable room-temperature single-photon emission at telecom wavelengths from sp3 defects in carbon nanotubes. *Nat. Photonics* **2017**, *11* (9), 577–582.
(7) Bourrellier, R.; et al. Bright UV Single Photon Emission at Point Defects in h-BN. *Nano Lett.* **2016**, *16* (7), 4317–4321.
(8) Tran, T. T.; et al. Quantum emission from hexagonal boron nitride monolayers. *Nat. Nanotechnol.* **2016**, *11* (1), 37–41.
(9) Chejanovsky, N.; et al. Structural Attributes and Photodynamics of Visible Spectrum Quantum Emitters in Hexagonal Boron Nitride. *Nano Lett.* **2016**, *16* (11), 7037–7045.
(10) Exarhos, A. L.; et al. Optical Signatures of Quantum Emitters in Suspended Hexagonal Boron Nitride. *ACS Nano* **2017**, *11* (3), 3328–3336.
(11) Srivastava, A.; et al. Optically active quantum dots in monolayer WSe2. *Nat. Nanotechnol.* **2015**, *10* (6), 491–496.
(12) He, Y.-M.; et al. Single quantum emitters in monolayer semiconductors. *Nat. Nanotechnol.* **2015**, *10* (6), 497–502.
(13) Chakraborty, C.; et al. Voltage-controlled quantum light from an atomically thin semiconductor. *Nat. Nanotechnol.* **2015**, *10* (6), 507–511.
(14) Koperski, M.; et al. Single photon emitters in exfoliated WSe2 structures. *Nat. Nanotechnol.* **2015**, *10* (6), 503–506.
(15) Zhao, H.; Pettes, M. T.; Zheng, Y.; Htoon, H. Site-controlled telecom-wavelength single-photon emitters in atomically-thin MoTe2. *Nat. Commun.* **2021**, *12* (1), 6753.
(16) Palacios-Berraquero, C.; et al. Large-scale quantum-emitter arrays in atomically thin semiconductors. *Nat. Commun.* **2017**, *8* (1), 15093.
(17) Li, H.; et al. Optoelectronic crystal of artificial atoms in strain-textured molybdenum disulphide. *Nat. Commun.* **2015**, *6* (1), 7381.
(18) Branny, A.; Kumar, S.; Proux, R.; Gerardot, B. D. Deterministic strain-induced arrays of quantum emitters in a two-dimensional semiconductor. *Nat. Commun.* **2017**, *8* (1), 15053.
(19) Guinea, F.; Katsnelson, M. I.; Geim, A. K. Energy gaps and a zero-field quantum Hall effect in graphene by strain engineering. *Nat. Phys.* **2010**, *6* (1), 30–33.
(20) Naumis, G. G.; Barraza-Lopez, S.; Oliva-Leyva, M.; Terrones, H. Electronic and optical properties of strained graphene and other strained 2D materials: a review. *Rep. Prog. Phys.* **2017**, *80* (9), 096501.
(21) Xia, F.; et al. Two-dimensional material nanophotonics. *Nat. Photonics* **2014**, *8* (12), 899–907.
(22) Bonaccorso, F.; Sun, Z.; Hasan, T.; Ferrari, A. C. Graphene photonics and optoelectronics. *Nat. Photonics* **2010**, *4* (9), 611–622.
(23) Koppens, F. H. L.; et al. Photodetectors based on graphene, other two-dimensional materials and hybrid systems. *Nat. Nanotechnol.* **2014**, *9* (10), 780–793.
(24) Aharonovich, I.; Englund, D.; Toth, M. Solid-state single-photon emitters. *Nat. Photonics* **2016**, *10* (10), 631–641.
(25) Wang, Q.; et al. Highly Polarized Single Photons from Strain-Induced Quasi-1D Localized Excitons in WSe2. *Nano Lett.* **2021**, *21* (17), 7175–7182.
(26) Kumar, S.; Kaczmarczyk, A.; Gerardot, B. D. Strain-Induced Spatial and Spectral Isolation of Quantum Emitters in Mono- and Bilayer WSe2. *Nano Lett.* **2015**, *15* (11), 7567–7573.
(27) Rosenberger, M. R.; et al. Quantum Calligraphy: Writing Single-Photon Emitters in a Two-Dimensional Materials Platform. *ACS Nano* **2019**, *13* (1), 904–912.
(28) Lee, H.; et al. Drift-dominant exciton funneling and trion conversion in 2D semiconductors on the nanogap. *Sci. Adv.* **2022**, *8* (5), No. eabm5236.
(29) Kim, S.-S.; et al. Strain-Assisted Wafer-Scale Nanoperforation of Single-Layer Graphene by Arrayed Pt Nanoparticles. *Chem. Mater.* **2015**, *27* (20), 7003–7010.
(30) Conley, H. J.; et al. Bandgap Engineering of Strained Monolayer and Bilayer MoS2. *Nano Lett.* **2013**, *13* (8), 3626–3630.
(31) He, K.; Poole, C.; Mak, K. F.; Shan, J. Experimental Demonstration of Continuous Electronic Structure Tuning via Strain in Atomically Thin MoS2. *Nano Lett.* **2013**, *13* (6), 2931–2936.
(32) Muoi, D.; et al. Electronic properties of WS2 and WSe2 monolayers with biaxial strain: A first-principles study. *Chem. Phys.* **2019**, *519*, 69–73.
(33) Darlington, T. P.; et al. Imaging strain-localized excitons in nanoscale bubbles of monolayer WSe2 at room temperature. *Nat. Nanotechnol.* **2020**, *15* (10), 854–860.
(34) Aljarb, A.; et al. Ledge-directed epitaxy of continuously self-aligned single-crystalline nanoribbons of transition metal dichalcogenides. *Nat. Mater.* **2020**, *19* (12), 1300–1306.
(35) Albagami, A.; et al. Tip-Enhanced Photoluminescence of Freestanding Lateral Heterobubbles. *ACS Appl. Mater. Interfaces* **2022**, *14* (8), 11006–11015.
(36) Xiao, D.; et al. Coupled Spin and Valley Physics in Monolayers of ${\mathrm{MoS}}_{2}$ and Other Group-VI Dichalcogenides. *Phys. Rev. Lett.* **2012**, *108* (19), 196802.
(37) Liu, G.-B.; et al. Three-band tight-binding model for monolayers of group-VIB transition metal dichalcogenides. *Phys. Rev. B* **2013**, *88* (8), 085433.
(38) Kośmider, K.; González, J. W.; Fernández-Rossier, J. Large spin splitting in the conduction band of transition metal dichalcogenide monolayers. *Phys. Rev. B* **2013**, *88* (24), 245436.
(39) Zhang, X.-X.; You, Y.; Zhao, S. Y. F.; Heinz, T. F. Experimental Evidence for Dark Excitons in Monolayer WSe_2. *Phys. Rev. Lett.* **2015**, *115* (25), 257403.
(40) Zhang, X.-X.; et al. Magnetic brightening and control of dark excitons in monolayer WSe2. *Nat. Nanotechnol.* **2017**, *12* (9), 883–888.
(41) Li, Z.; et al. Emerging photoluminescence from the dark-exciton phonon replica in monolayer WSe2. *Nat. Commun.* **2019**, *10* (1), 2469.
(42) Feierabend, M.; Khatibi, Z.; Berghäuser, G.; Malic, E. Dark exciton based strain sensing in tungsten-based transition metal dichalcogenides. *Phys. Rev. B* **2019**, *99* (19), 195454.
(43) Park, K.-D.; et al. Radiative control of dark excitons at room temperature by nano-optical antenna-tip Purcell effect. *Nat. Nanotechnol.* **2018**, *13* (1), 59–64.
(44) Ye, Z.; et al. Efficient generation of neutral and charged biexcitons in encapsulated WSe2 monolayers. *Nat. Commun.* **2018**, *9* (1), 3718.
(45) Zhang, X.; et al. Diffusion-Controlled Epitaxy of Large Area Coalesced WSe2Monolayers on Sapphire. *Nano Lett.* **2018**, *18* (2), 1049–1056.

https://doi.org/10.1021/acsnano.2c02974
ACS Nano 2022, 16, 9651–9659